JACS
JOURNAL OF THE AMERICAN CHEMICAL SOCIETY
Article
pubs.acs.org/JACS

Ambient Stable Tetragonal and Orthorhombic Phases in Penta-Twinned Bipyramidal Au Microcrystals

Gangaiah Mettela,[†] Meha Bhogra,[‡] Umesh V. Waghmare,[‡] and Giridhar U. Kulkarni*[,†]

[†]Thematic Unit of Excellence on Nanochemistry and Chemistry and Physics of Materials Unit and [‡]Theoretical Sciences Unit, Jawaharlal Nehru Centre for Advanced Scientific Research (JNCASR), Jakkur P.O., Bangalore 560 064, India

Supporting Information

ABSTRACT: Face-centered cubic (fcc) lattice is the only known crystal structure of bulk gold. In the present work, we report the presence of body-centered tetragonal (bct) and body-centered orthorhombic (bco) phases in bipyramidal Au microcrystals with penta-twinned tips. These microcrystals have been obtained by thermolysis of $(AuCl_4)^-$ stabilized with tetraoctylammonium bromide (ToABr) in air at about 220 °C for 30 min. Using a laboratory monochromatic X-ray source, the non-fcc phases could be readily detected. The remarkable occurrence of non-fcc phases of Au grown in the temperature window of 200−250 °C results from the geometrically induced strains in the bipyramids. Having derived first-principles theoretical support for the temperature-dependent stability of non-fcc Au structures under stress, we identify its origin in *soft* modes. Annealing at high temperatures relieves the stress, thus destabilizing the non-fcc phases.

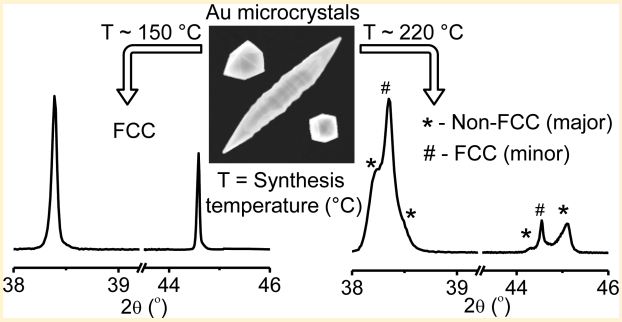

INTRODUCTION

Cubic lattice structure preferred by noble metals (e.g., Au, Ag, Pd and Pt) is thermodynamically highly stable. Lower-symmetry crystal structures are not known to stabilize relative to the face-centered cubic (fcc) bulk even at high pressures.[1] Observing a structural transformation in these metals is therefore fundamentally exciting and can be possibly useful in tuning their otherwise noble behavior. Recent explorations in this direction have focused on nanocrystals, as the energy needed for lattice distortion is relatively low when the size is a few nanometers.[2,3] The presence of structural defects can further contribute to their stability.[4]

Among the possible metastable phases, hexagonal close packed (hcp) structure is quite prevalent in Ag nanoparticles[4−13] under ambient conditions, but rather infrequent in Au nanoparticles[14−17] (Supporting Information, Table S1). Under high pressure, body-centered tetragonal (bct) and trigonal phases have been identified in Ag and Pd nanoparticles using high-energy X-ray diffraction (XRD) and selective area electron diffraction (SAED) (see Table S1).[2,18,19] Au nanocrystals are not known to exhibit such phases even under pressure. However, fcc to bct phase transformation has been observed in small regions of Au nanocrystals under transmission electron microscope (TEM) during tensile fracture.[20,21]

Among the larger crystallites exhibiting lattice distortion, penta-twinned Ag nanowires are the most prominent.[22] Along the length, the nanowire is enclosed with five {100} facets, while its tips are made of five {111} facets hosting twin planes at each boundary.[23] It is proposed that the strain associated with twinning can give rise to body-centered orthorhombic (bco)[24] or bct[25] structure. The presence of bct phase in Ag nanowires has been confirmed using high-energy X-ray synchrotron measurements.[26,27] The internal strain induced by penta-twinning seems to grow with the lateral dimension of the nanowire making larger diameters implausible.[28]

There have been theoretical investigations as well. An atomistic study of thin Au nanowires has revealed a stress-induced fcc to bct transformation for ⟨100⟩ orientation when external pressure is above 1 GPa.[29] While the elastic stability of the bct phase is still debated,[30] thermal vibrations can cause fcc ⟨100⟩ orientation to transform to bct.[31,32] Recently, large-scale simulations of 5-fold twinned nanowires using modified embedded atom method have shown the occurrence of bco phase induced by large internal stresses concentrated at twin boundaries.[30] Further, internal strains developed in nanowires have been shown to get relieved through the generation of dislocations, thus hindering the phase transition.[31]

We have been exploring the possibility of inducing non-fcc phase formation in highly twinned Au microcrystals, which in our previous study were obtained in fcc under certain synthetic conditions.[33] In this work, we have optimized the synthetic conditions aiming to stabilize non-fcc phases. The present study has thus revealed the remarkable presence of significant proportions of bco and bct phases in Au bipyramids at ambient pressures, which could be detected easily using a laboratory X-ray diffraction (XRD) equipment. Through first-principles

Received: December 3, 2014
Published: February 11, 2015

DOI: 10.1021/ja512340m
J. Am. Chem. Soc. 2015, 137, 3024−3030

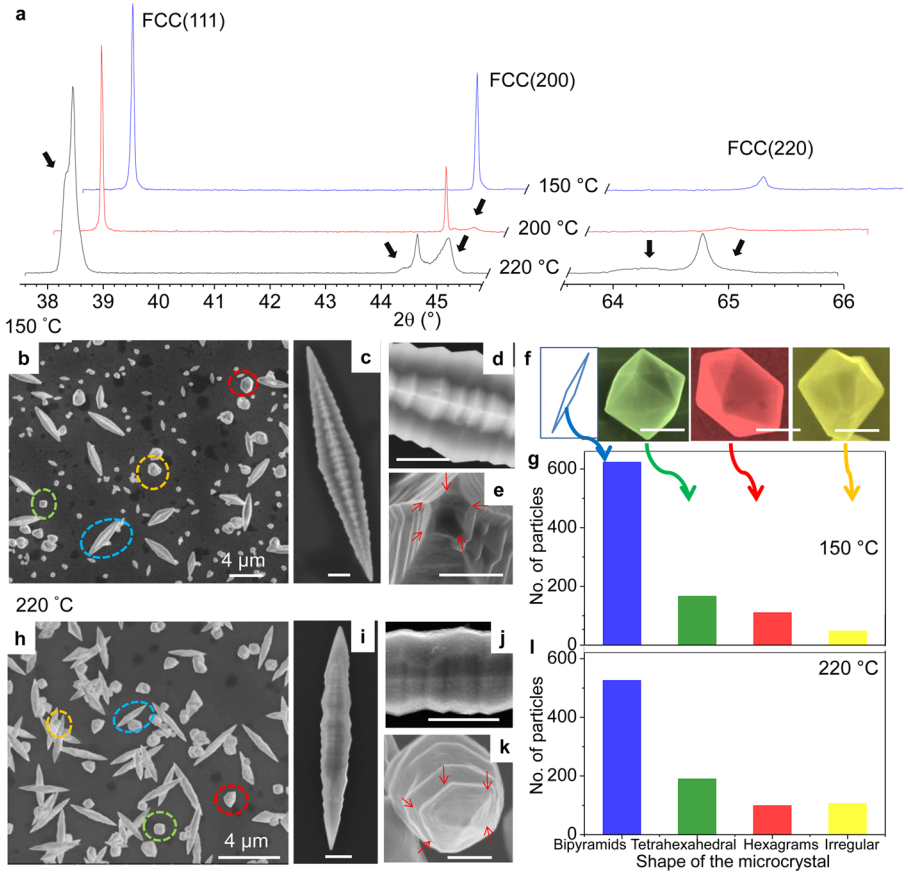

Figure 1. (a) XRD patterns obtained from Au microcrystals prepared at 150, 200, and 220 °C. Black arrows indicate features arising out of distortions from the fcc cell. SEM images of Au microcrystals, prepared at (b) 150 °C and (h) 220 °C. Other images (c–e and i–k) correspond to different magnifications and orientations of bipyramids. (f) Typical magnified images of nonbipyramidal particles. Histograms of particle counts from (g) 150 °C and (l) 220 °C preparations. Scale bar where not indicated is 500 nm.

theoretical study of temperature-dependent free energies of elastic distortions in the fcc structure, we show the presence of such phases and also present a soft mode-based mechanism that captures the trends in the stability of non-fcc phases of noble metals, in general.

METHODS

Chemicals and Synthesis of AuAgToABr. Hydrogen tetrachloroaurate(III) hydrate ($HAuCl_4 \cdot 3H_2O$), silver nitrate ($AgNO_3$), tetraoctylammonium bromide (ToABr), and toluene were obtained from Spectrochem, India and used without further purification. Double-distilled water used throughout this investigation. A 0.75 mL of $HAuCl_4$ (25 mM), 3 mL of ToABr in toluene (50 mM), and 0.5 mL of $AgNO_3$ (25 mM) were added and stirred for 10 h for effective phase transfer of the metal ions to the organic medium. The organic layer, henceforth called AuAgToABr precursor solution, was separated and used immediately. The substrates, Si, glass, and quartz were cleaned with water, IPA, toluene, and dried under N_2 gas.

Characterization. Scanning electron microscopy (SEM) imaging and energy-dispersive X-ray spectra was performed using a Nova NanoSEM 600 equipment (FEI Co., The Netherlands). TEM measurements were carried out with a JEOL-3010 instrument operating at 300 kV. XRD measurements were performed using a PANalytical instrument (Cu Kα, 1.5406 Å; scan rate, 1°/3 min). X-ray photoelectron spectroscopy (XPS) measurements were performed using a Omicron instrument (Al Kα = 1486.6 eV). Thermogravimetric analysis (TGA) was carried out using a Mettler Toledo, TG-850 instrument in N_2 atmosphere.

Computational Details. Our calculations are based on first-principles density functional theory (DFT) as implemented in Quantum Espresso (QE) package[34] with Perdew–Zunger[35] functional of the exchange–correlation energy approximated with a local density approximation (LDA). The interaction between ionic core and valence electron is represented with projector augmented wave (PAW) method.[36] Plane-wave basis set is truncated with an energy cutoff of 40 Ry in the expansion of Kohn–Sham wave functions (and a corresponding cutoff of 400 Ry for charge density), and integrations over Brillouin Zone are sampled with a uniform 24 × 24 × 16 k-mesh for the bct type of unit cell.

The elastic constants of fcc Au were calculated using energy-strain approach as

$$C_{ij} = \frac{1}{V_o}\frac{\partial^2 E_{\text{total}}}{\partial \epsilon_i \partial \epsilon_j}$$

where E_{total} is the total energy, V_o is the volume of unit cell and ϵ_i is the strain in Voigt notation. For normal strains, the elastic compliance matrix with cubic symmetry is written as

$$\mathbf{C} = \begin{pmatrix} C_{11} & C_{12} & C_{12} \\ C_{12} & C_{11} & C_{12} \\ C_{12} & C_{12} & C_{11} \end{pmatrix}$$

with C_{11} and C_{12} as independent constants.

Dynamical matrices (DMs) and phonon frequencies are obtained using the DFT linear response method[37] on a uniform 4 × 4 × 2 mesh of q-points, which are Fourier interpolated to wave vectors on a finer mesh used in determination of Helmholtz free energies as a function of temperature and strain within a harmonic approximation:

DOI: 10.1021/ja512340m
J. Am. Chem. Soc. 2015, 137, 3024–3030

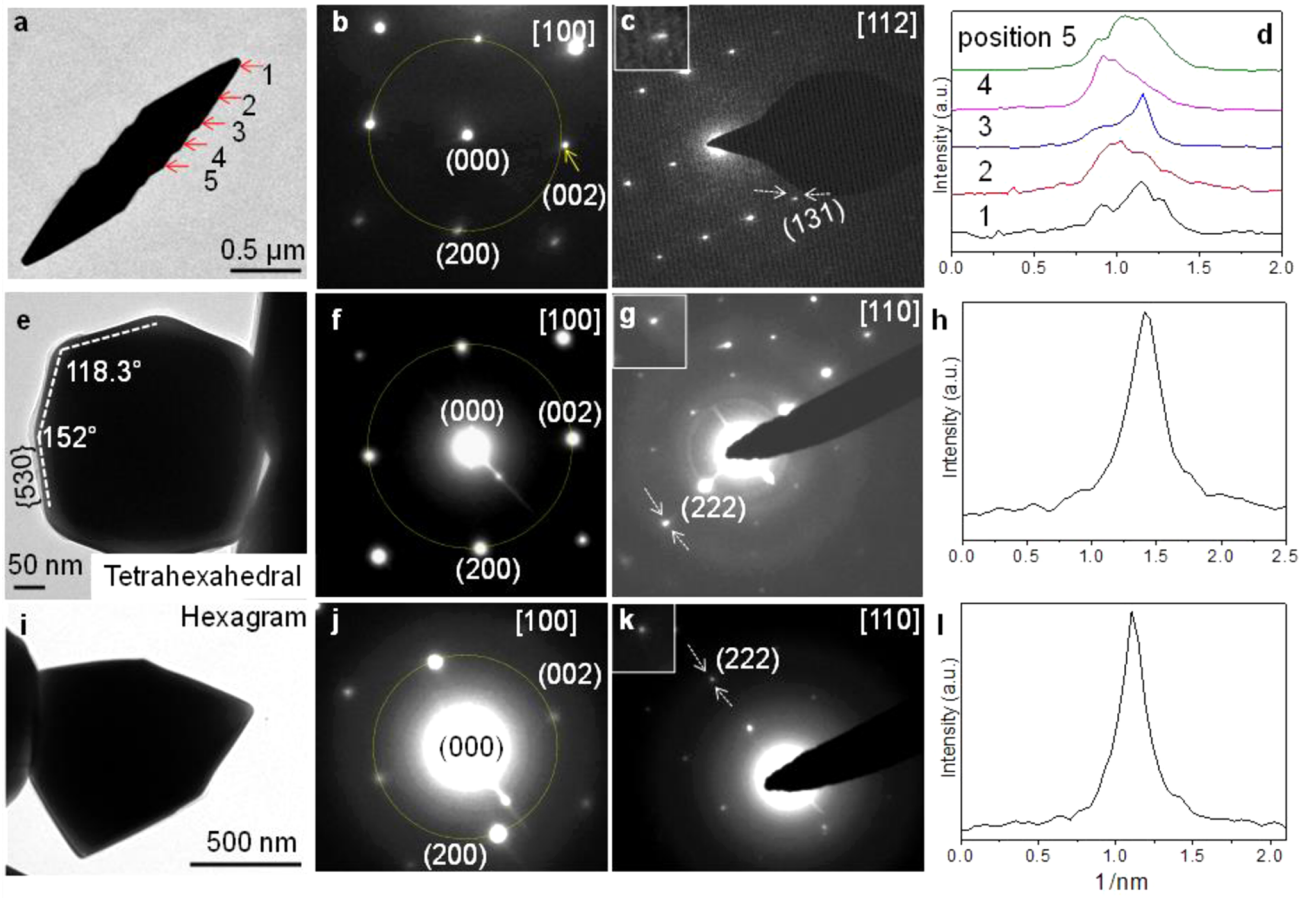

Figure 2. (a–c) TEM image of Au bipyramid and the ED patterns collected along the [100] and [112] directions. (d) Intensity profiles drawn along {113} spots from the regions 1 to 5 shown in (a). (e, i) TEM images of Au tetrahexahedral and hexagram microcrystals, and their respective ED patterns collected along the [100] (f, j) and [110] (g, k) directions. (h) The intensity profile of (222) spot shown in (g) and (l) of that shown in (k). The tetrahexahedral microcrystal shown in (e) is enclosed with the fcc{530} facets (see Figure S9).

$$A(T, \varepsilon) = E_{\text{total}} + \frac{k_B T}{N_q} \sum_{i,q} \log\left[2\sinh\left(\frac{\hbar\omega_{iq}}{2k_B T}\right)\right]$$

where N_q is the number of q-points on 24 × 24 × 16 mesh in the Brillouin Zone (BZ), ω_{iq} is the frequency at a wave vector $\mathbf{q}$.

RESULTS

Stabilizing the Non-fcc Phases. We prepared penta-twinned Au microcrystals by subjecting few drops of AuAgToABr solution to different thermolysis temperatures on Si substrates (see Figure 1 and Methods section). XRD patterns of the obtained crystallites showed something striking (Figure 1a). While the 150 °C preparation showed sharp and symmetrical peaks that are indexable to bulk fcc with a lattice parameter of 4.081 Å (Au, 4.0804 Å, ICSD No. 180868), the diffraction pattern obtained from microcrystals prepared at 200 °C was not quite the same. Although all intense peaks correspond to bulk fcc structure, we see the emergence of new peak adjacent to fcc(200) at a slightly higher 2θ value (45.05°). Amazingly, all fcc peaks are seen considerably asymmetric and broad with the 220 °C preparation, some even exhibiting clear splitting near fcc(200) and (220). The peak shapes encountered here may be compared with those of penta-twinned Ag nanowires obtained using a high-resolution synchrotron source.[26] It appears that in our study, the Au microcrystals synthesized at 220 °C host significant amounts of non-fcc phases.[38] Similar peak shapes have been observed under high pressures in other noble fcc metals.[18]

To understand the morphological aspects of Au bipyramids hosting non-fcc phases, we have carried out SEM analysis of the microcrystals (Figure 1). From the SEM images in Figure 1b,h corresponding to synthetic temperatures of 150 and 220 °C, respectively, we see, besides bipyramidal shaped particles (shown in blue circles), tetrahexahedral (green), hexagrams (red) and irregular microcrystals (yellow). The average lengths of bipyramids prepared at 150 and 220 °C are 5.5 and 3.5 μm, respectively (see Figure 1c,i), which are enclosed with penta-twinned tips (Figure 1e,k). In contrast to 150 °C preparation, the bipyramids obtained at 220 °C has roughened surface, and the edges are slightly rounded (Figure 1d,j) perhaps due to rapid reduction of AuAgToABr at higher synthetic temperature. The bipyramid grows along the ⟨110⟩ direction starting from a decahedron by enclosing a highly corrugated region in between the penta-twinned tips (Figure S1), as detailed out in our previous study.[33]

Based on TEM analysis, the corrugations have been assigned to high index facets, {hk0} where h or $k \geq 2$ (see Figure S2). Magnified images of the non-bipyramidal particles are shown in Figure 1f, where the irregular particle (image on the right) seems to exhibit a penta-twinned geometry on one side. From the histograms in Figure 1g,l, we see that in both cases, the major product is bipyramids (~65% and ~57%, respectively,

DOI: 10.1021/ja512340m
J. Am. Chem. Soc. 2015, 137, 3024–3030

for 150 and 220 °C thermolysis) with tetrahexahedral (17% and 20%), hexagram (12% and 10%), and irregular particles (5% and 11%) as minor products. Interestingly, tetrahexahedral and hexagram crystallites observed in our study are relatively larger (~1 μm) compared to previous studies (see Figure 1f and Table S2).

In our previous study,[33] it is discussed in detail how Ag(I) assists the bipyramidal morphology while not being part of the structure (see Figure S3). Residual Ag from precursor, which is surface bound, could be easily washed away not influencing the morphology and the non-fcc phases (see Figure S4). Further, the bipyramidal morphology hosting non-fcc phases is found to be independent of the nature of the substrate employed (see Figure S5). However, the nature of the halide ion seems to matter (see Figure S6).

TEM Characterization. SAED was performed on different microcrystals from the 220 °C preparation (Figure 2). Although the ED pattern obtained along the [100] direction (Figure 2b) of a bipyramid (Figure 2a) exhibits a nearly square symmetry, the *d*-spacings for the (002) and (200) reflections differ by ~3% (2.08 and 2.01 Å, respectively), in contrast to the equal *d*-spacings observed from the 150 °C preparation (Figure S7 and Table S3). The observed difference in the former case is similar to the reported value in Ag nanowires.[26] Such deviations from symmetry indicate the presence of non-fcc phases in the bipyramid. ED patterns along the [112] axis have been collected between the tip and the center at an interval of 200 nm. In all the cases, we observed that the {113} and {220} spots exhibited splitting in the intensity profiles (Figures 2d and S8). It implies that the non-fcc phases are distributed allover, from tip to the center of the Au bipyramid. In tetrahexahedral (Figure 2e–h) and hexagram (Figure 2i–l) particles, neither non-uniform *d*-spacings nor non-uniform spots are observed. The surface induced strain, if any, should also be minimal in these microcrystals unlike in nanocrystals of similar shapes.[39]

Having clues for the presence of non-fcc phase(s), we attempted fitting the XRD patterns with combinations of crystal structures, iteratively using the WinPLOTR software. After several trials (Figures S10 and S11), we embarked on three phase combinations among which, fcc + tetragonal (*I*4/*mmm*) + orthorhombic (*Immm*), produced the best fit with χ^2 of 3.16 (Figure 3).

XRD peak analysis revealed the presence of non-fcc phases with compression along *c*-axis and expansion along *a* and *b* axes. Figure 3a shows the schematic of fcc, derived FCT along with bct unit cells. Note that for bct, $a' = b' = a/\sqrt{2}$ and $c' = c$, where *a*, *b*, and *c* are lattice parameters of FCT. For bct form of fcc, $c'/a' = \sqrt{2}$. Experimentally obtained lattice parameters of the bct are, $a' = b' = 2.9062$ Å and $c' = 4.0503$ Å with $c'/a' = 1.394$ (deviation of −1.44% from the fcc structure). Unequal strains along *a*, *b*, and *c* axes result in a bco structure. The calculated lattice parameters of bco are $a' = 2.9165$, $b' = 2.8907$, and $c' = 4.0337$ Å with $c'/a' = 1.383$ and $c'/b' = 1.395$ which indicate that the strain along the *a*-axis is higher than that along *b*.[40] Finally, in terms of cell volume, bct volume is 0.62% higher, while that of bco is higher by only 0.03% with reference to the unstrained bct ($c'/a' = \sqrt{2}$) (see Table S4).

As shown in Figure 3b, the asymmetrically broadened profile of the $(111)_C$ peak is fitted with $(101)_T$, $(101)_O$, and $(011)_O$ peaks. The non-fcc peaks are broader (particularly from bct) due to the strain prevalent in these unit cells. This is more evident in the $(200)_C$ region where the non-fcc contribution is seen well separated, which has been fitted to $(002)_T$ and

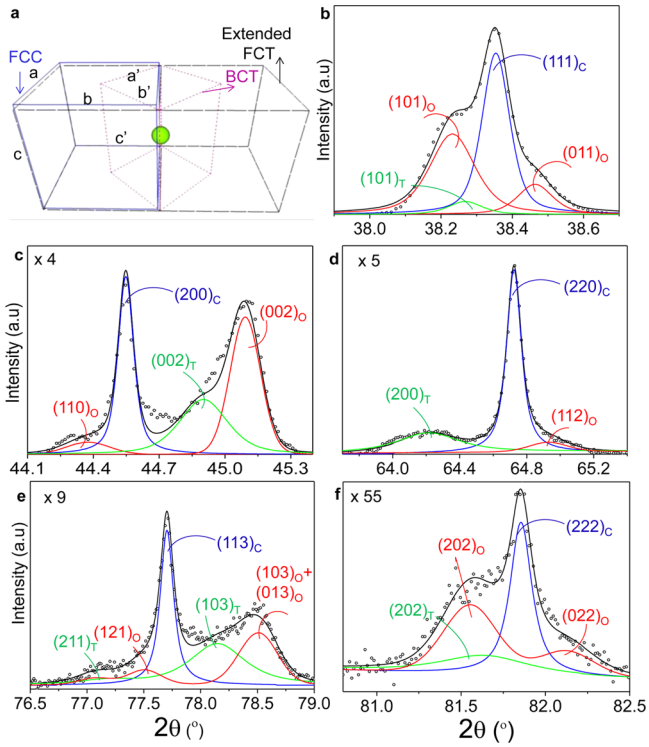

Figure 3. (a) Schematic illustrating fcc unit cell along with extended FCT and bct unit cells. (b–f) Profile fitting of XRD peaks. The experimental data is in black circles. Blue, red, and green fitted curves represent cubic (marked as C), orthorhombic (O), and tetragonal (T) peaks, respectively, with their sum shown as a black curve.

$(002)_O$ peaks (Figure 3c). Indeed, the order of the peaks represents increasing compression of the *c*-axis. For instance, bct(002) reflection appears in between fcc(002) and bco(002) such that the order of *c* is $c_{fcc} > c_{bct} > c_{bco}$. Similar trends are seen in the other regions as well (see Figure 3d–f).

Based on the areas under the XRD peaks, we estimated the relative contributions of the different phases as fcc (46.7%), bct (16.94%), and bco (36.30%). Based on TEM results (Figure 2), it is clear that the non-fcc fraction (bct + bco = 53.3%) comes mainly from the Au bipyramid, while other shaped particles contribute to the fcc fraction. These proportions are sensitive to the synthetic temperature (Figure 4a). Only around 220 °C thermolysis, the (bco + bct)/fcc ratio is significant; at lower or higher thermolysis temperatures the non-fcc phases formation is not favored (see Figures 1 and S12). This trend may be related to the pace of thermolysis at different temperatures. From the isothermal TGA data collected at 150 °C (Figure S13), we see that the weight loss was gradual, and a steady state was not reached even after 720 min, indicating a slow decomposition of the precursor. With 200 °C TGA, complete decomposition occurred at around ~300 min to reach a steady weight of ~7% of the initial. The time taken to reach the steady state decreased rapidly at higher TGA temperatures, as shown in Figure 4a. Interestingly, the change in this trend occurs around ~200 °C similar to the change seen with the (bco + bct)/fcc ratio. At lower temperatures (<200 °C), the precursor decomposition and hence bipyramid growth is slow, and the stress developed due to penta-twinning could be accommodated in the fcc lattice itself. At much higher temperatures, though the growth of bipyramid is faster, the internal stresses get annealed due to the abundant thermal energy available. In

DOI: 10.1021/ja512340m
J. Am. Chem. Soc. 2015, 137, 3024–3030

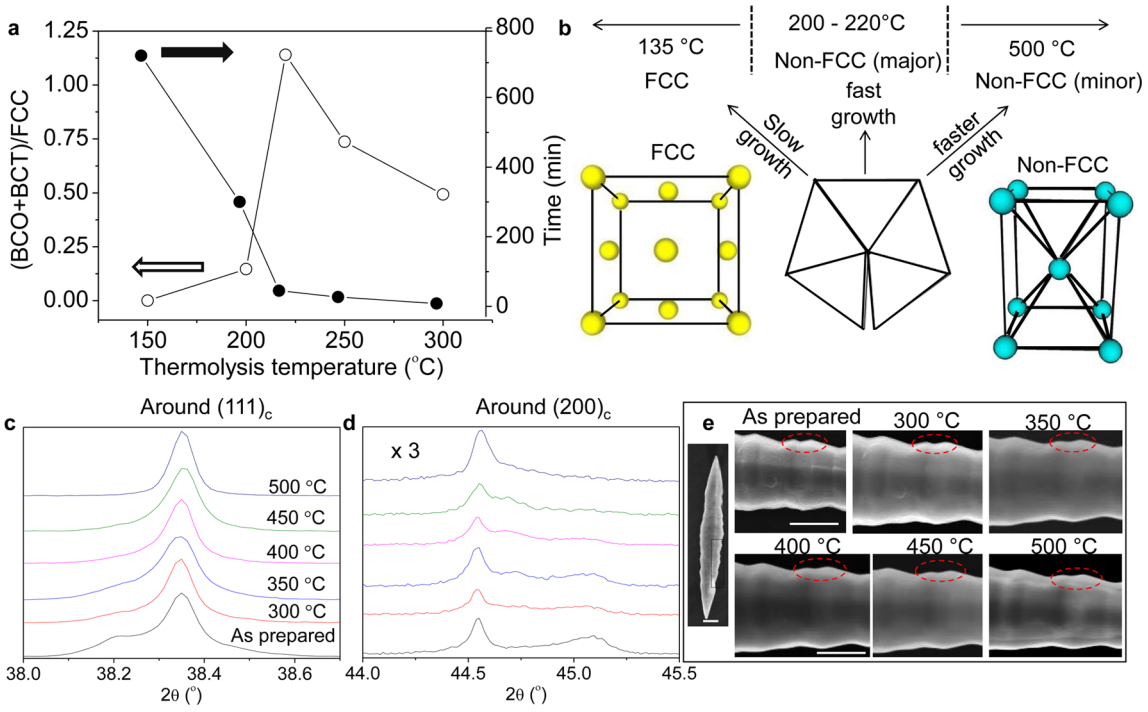

Figure 4. (a) Variation in the non-fcc/fcc ratio as derived from XRD peak areas for microcrystals synthesized at various thermolysis temperatures. The time taken to reach a steady wt % in TGA is also shown in each case. (b) Schematic illustrating the occurrence of non-fcc and fcc phases in Au bipyramids at low and high thermolysis temperatures. (c, d) XRD patterns from Au microcrystals annealed at various temperatures. (e) SEM images of a bipyramid on annealing at various temperatures. Scale bar, 500 nm. Annealing was carried out for 1 h in air at each temperature, and the measurements were done after cooling to room temperature.

the intermediate temperature range (~200−250 °C) however, the thermal annealing seems incompetent to cope up with the speedy growth leading to preservation of the strain in the form of non-fcc phases (Figure 4b) which begin to nucleate even at small sizes (Figure S14). Like in the case of Ag nanowires,[26] the non-fcc phases may reside at the core, while fcc forms the shell.

It is noteworthy that these interesting non-fcc phases in Au bipyramid are highly stable in ambient conditions (Figure S15). Their stability under harsh chemical environments and e-beam conditions is already established (see Figure S4), the latter aspect assumes significance with regard to hcp Au nanosheets.[15] However, the strain in the bipyramids could be released by annealing at elevated temperatures (see Figure 4c,d) with little change in morphology (Figures 4e and S16). The XRD pattern obtained at 500 °C is indexable entirely to fcc. The conversion to fcc results in the reduction of volume of non-fcc unit cells, which in turn reduced the length and width of the bipyramid by 6.12% and 4.54%, respectively (Figure S17).

Theoretical Study. We now analyze the non-fcc (bct and bco) phases of Au bipyramids (Figures 3 and 4) treating them as strained forms of its fcc structure using first-principles calculations. The structural response governing these small strains (within 2%) is determined by elastic moduli (see Table 1) of fcc Au (see Supporting Information, Section II). Two soft modes of deformation of fcc Au, revealed by eigenvectors of the elastic compliance matrix **C**, are $\vec{d}_1 \equiv \varepsilon_{xx} = \varepsilon_{yy} = -(\varepsilon_{zz}/2)$ and $\vec{d}_2 \equiv \varepsilon_{xx} = -\varepsilon_{yy}$, $\varepsilon_{zz} = 0$. The former results in a bct structure, while the latter (or a linear combination of the two) results in a bco structure. The structures resulting from imposed strains along $\vec{d}_1$ and $\vec{d}_2$ have lower energies at 0 K than the other strained bct and bco configurations (including the ones revealed by XRD analysis) (see Figure S18).

Table 1. Elastic Properties of Fcc Noble Metals[43]

metal	C_{11} (GPa)	C_{12} (GPa)	C_{44} (GPa)	$C_{11} - C_{12}$ (C') (GPa)	$(C_{11} - C_{12})/(C_{11} + 2C_{12})$
Au	**210**	**177**	45	33	0.058
Ag	132	97	51	35	0.107
Pd	234	176	72	58	0.098
Pt	358	254	77	104	0.120

Note: The values in **bold** are determined in the present work.

Analysis of vibrational spectra of the strained configurations supports the observation of non-fcc (bct and bco) phases with $c'/a' < \sqrt{2}$ in Au microcrystals. Configurations with strain $\vec{d}_1$, bct I ($\varepsilon_{xx} = 0.006$, $\varepsilon_{yy} = 0.006$, $\varepsilon_{zz} = -0.012$) and bct II ($\varepsilon_{xx} = -0.006$, $\varepsilon_{yy} = -0.006$, $\varepsilon_{zz} = 0.012$), show softening of the longitudinal acoustic (LA) modes (Mode I in Figure 5b) along $\Gamma - S$ (1/2,1/2,0) in bct I and hardening in bct II (Figure 5a), suggesting possible stabilization of bct I (with negative ε_{zz}) through thermal fluctuations in the $a'-b'$ plane (Figure 3a). Deformation $\vec{d}_2$ present in bco I ($\varepsilon_{xx} = 0.005$, $\varepsilon_{yy} = -0.005$, $\varepsilon_{zz} = 0.0$) preserves the volume of fcc structure and thus shows negligible changes in the vibrational spectra (see Figure S19). The observed non-fcc phases, bct III ($\varepsilon_{xx} = 0.007$, $\varepsilon_{yy} = 0.007$, $\varepsilon_{zz} = -0.008$) and bco II ($\varepsilon_{xx} = 0.011$, $\varepsilon_{yy} = 0.002$, $\varepsilon_{zz} = -0.012$), with $c'/a' < \sqrt{2}$ exhibit significant softening of LA mode along $\Gamma - S$ (see mode I in Figure 5b) and transverse acoustic (TA) modes along $\Gamma - T$ (1/2,0,1/2) and $\Gamma - U$ (0, 1/2,1/2) directions (Figure 5d), indicating their stabilization through shear strain (ε_{xz}) fluctuations (mode II in Figure 5c). In addition, bct III shows softening of high-energy optical modes

DOI: 10.1021/ja512340m
J. Am. Chem. Soc. 2015, 137, 3024−3030

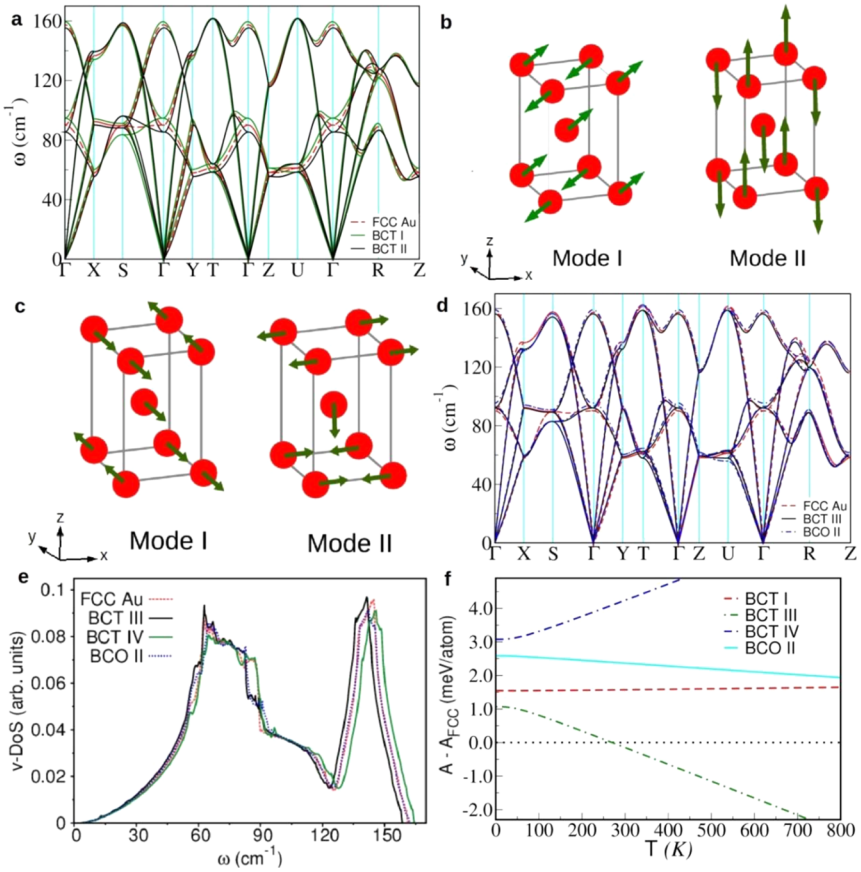

Figure 5. (a) Phonon spectra of fcc, bct I, and bct II configurations; (b) eigenvectors of low-energy acoustic modes at S(1/2,1/2,0) point (mode I softens in bct I and hardens in bct II); (c) eigenvectors of low-energy transverse acoustic modes at T(1/2,0,1/2) point; (d) phonon spectra of bct III and bco II; (e) phonon density of states (v-DoS) of non-fcc configurations compared with that of fcc Au; and (f) vibrational contribution to free energies of non-fcc configurations with reference to the fcc structure of Au at finite temperatures (dotted line at 0.0 meV/atom represents the fcc structure).

(120−160 cm^{-1}). An increase in the number of low-frequency modes of non-fcc configurations with $c'/a' < \sqrt{2}$ (bct I, bct III and bco II) and decrease for $c'/a' > \sqrt{2}$ (bct IV: $\varepsilon_{xx} = -0.007$, $\varepsilon_{yy} = -0.007$, $\varepsilon_{zz} = 0.008$) are evident in density of vibrational states (Figure 5e).

The contribution of soft vibrational modes (Figure 5d) to free energies of the non-fcc configurations is significant and stabilizes them at finite temperatures ($T > 300$ K), supporting the occurrence of certain bct and bco phases (bct III and bco II) in geometrically strained Au bipyramid through thermal activation (see Figure 5f). This is in contrast to the bct IV configuration ($c'/a' > \sqrt{2}$) which destabilizes with temperature, clearly showing a strong effect of c'/a' ratio on the stability of strained phases. The free energies of configurations with strains along $\vec{d}_1$ and $\vec{d}_2$ remain almost unchanged by thermal effects. This can be traced to negligible stresses in the configurations obtained with $\vec{d}_1$ and $\vec{d}_2$ modes of deformation, but higher induced stresses in bct III, bct IV and bco II structures (σ_{xx} of −1.3, 1.5, and −0.8 GPa respectively). Thus, the induced deviatoric stresses are relevant to thermal stabilization of non-fcc phases of Au with ($c'/a' < \sqrt{2}$). Devoid of geometrically induced strains, tetrahexahedral and hexagram particles of Au[41] do not exhibit any non-fcc phases.

Annealing at elevated temperatures releases the internal stresses in Au bipyramids through relaxation of strains associated with the bct and bco structures. Within the elastic range, the smaller the induced stresses, the slower is the rate of relaxation of strains.[42] Thus, reduction of non-fcc phases to stress-free fcc Au on annealing occurs at relatively high temperatures (∼500 °C).

The relevance of vibrations to non-fcc phases of Au was noticed earlier.[31] Soft vibrational modes identified here constitute elastic signatures relevant to fcc to non-fcc phase transition, which capture the trends in the stability of non-fcc phases in other noble metals. The lowest value of $(C_{11} - C_{12})/(C_{11} + 2C_{12})$ for Au (0.058) indicates its stronger tendency to undergo tetragonal (or orthogonal) distortion over uniform compression, when compared with other noble metals, namely, Ag, Pd, and Pt (see Table 1). Comparable values of $C_{11}-C_{12}$ or C' for Au and Ag suggest a feasibility of tetragonal phase in both these metals for small structures, consistent with the occurrence of bct phase in Ag nanowires observed at ambient pressure.[22] Lastly, higher shear elastic constant C_{44} of Ag, Pd, and Pt as compared to Au further suppresses the thermal stabilization of their non-fcc phases due to weaker contribution of the transverse (or shear) acoustic modes to free energy.

■ CONCLUSION

The present study involves thermalizing the precursor (AuAgToABr) in air to a range of thermolysis temperatures (150−220 °C). This yields distinctly shaped Au microcrystals, namely, bipyramids, tetrahexahedral, and hexagrams. The bipyramids are typically ∼3.5 μm long with a tip diameter of

DOI: 10.1021/ja512340m
J. Am. Chem. Soc. 2015, 137, 3024−3030

~120 nm and are faceted with a high index corrugated surface, with penta-twinned {111} facets at the tips. This five-fold symmetry along the length introduces internal strains, which are essentially absent in other shapes. Interestingly, the samples obtained above 200 °C (particularly at 220 °C) reveal the presence of non-fcc phases (bct (*I*4/*mmm*) and bco (*Immm*)) in significantly high proportions (~55%) at ambient pressure and can be easily detected using a laboratory monochromatic X-ray source. These non-fcc phases have been hitherto known to occur in nanowires or nanosheets of noble metals, only at high pressures. The kinetics of thermolysis seems to be critical in the existence of the non-fcc phases in Au bipyramids. At lower temperatures (<200 °C), the decomposition of the precursor being slow yields only the fcc phase in the bipyramids, while between 200 and 250 °C the reaction kinetics locks the strains to form the non-fcc phases. Annealing at higher temperatures (above 300 °C) unlocks the strains and results in nearly fcc phase at 500 °C. Theoretical calculations elucidate temperature dependence of the free energies of certain non-fcc (bct and bco) structures and highlight the role of internal stresses and relevance of soft modes in their stabilization. The analysis of elastic compliances reveals how $(C_{11} - C_{12})/(C_{11} + 2C_{12})$ singles Au out from the noble metals in its propensity to form bct and bco structures when subjected to stresses inherent to bipyramid form.

■ ASSOCIATED CONTENT

Supporting Information

Synthetic conditions, X-ray diffraction analysis, thermogravimetric analysis and DFT analysis. This material is available free of charge via the Internet at http://pubs.acs.org.

■ AUTHOR INFORMATION

Corresponding Author

*kulkarni@jncasr.ac.in

Notes

The authors declare no competing financial interest.

■ ACKNOWLEDGMENTS

The authors thank Nanomission DST, India for generous support. The authors thank Prof. C. N. R. Rao for his constant encouragement. We thank Mr. Anil, Mr. Vasudev, Mr. Jagadish, Dr. Jay Ghatak, and Mrs. Usha for their assistance in measurements. We thank Mr. Badari Narayana Rao for his assistance in profile fitting. G.M. thanks CSIR, India, for fellowship. U.V.W. acknowledges support from J. C. Bose National Fellowship of DST, Govt. of India.

■ REFERENCES

(1) McMahon, M. I.; Nelmes, R. J. *Chem. Soc. Rev.* **2006**, *35*, 943.

(2) Guo, Q.; Zhao, Y.; Wang, Z.; Skrabalak, S. E.; Lin, Z.; Xia, Y. *J. Phys. Chem. C* **2008**, *112*, 20135.

(3) Au cluster compounds are known to exhibit non-fcc metal clusters bonded with ligands. However they are a different class of materials. See for example Qian, H.; Eckenhoff, W. T.; Zhu, Y.; Pintauer, T.; Jin, R. *J. Am. Chem. Soc.* **2010**, *132*, 8280.

(4) Wang, B.; Fei, G. T.; Zhou, Y.; Wu, B.; Zhu, X.; Zhang, L. *Cryst. Growth Des.* **2008**, *8*, 3073.

(5) Aherne, D.; Ledwith, D. M.; Gara, M.; Kelly, J. M. *Adv. Funct. Mater.* **2008**, *18*, 2005.

(6) Bansal, V.; Li, V.; O'Mullane, A. P.; Bhargava, S. K. *CrystEngComm* **2010**, *12*, 4280.

(7) Zhelev, D. V.; Zheleva, T. S. *J. Appl. Phys.* **2014**, *115*, 044309.

(8) Liu, T.; Li, D.; Yang, D.; Jiang, M. *Chem. Commun.* **2011**, *47*, 5169.

(9) Liu, X.; Luo, J.; Zhu, J. *Nano Lett.* **2006**, *6*, 408.

(10) Singh, A.; Ghosh, A. *J. Phys. Chem. C* **2008**, *112*, 3460.

(11) Liang, H.; Yang, H.; Wang, W.; Li, J.; Xu, H. *J. Am. Chem. Soc.* **2009**, *131*, 6068.

(12) Liu, T.; Li, D.; Yang, D.; Jiang, M. *Langmuir* **2011**, *27*, 6211.

(13) Chakraborty, I.; Carvalho, D.; Shirodkar, S. N.; Lahiri, S.; Bhattacharyya, S.; Banerjee, R.; Waghmare, U.; Ayyub, P. *J. Phys.: Condens. Matter.* **2011**, *23*, 325401.

(14) Dubrovinsky, L.; Dubrovinskaia, N.; Crichton, W. A.; Mikhaylushkin, A. S.; Simak, S. I.; Abrikosov, I. A.; de Almeida, J. S.; Ahuja, R.; Luo, W.; Johansson, B. *Phys. Rev. Lett.* **2007**, *98*, 045503.

(15) Huang, X.; Li, S.; Huang, Y.; Wu, S.; Zhou, X.; Li, S.; Gan, C. L.; Boey, F.; Mirkin, C. A.; Zhang, H. *Nat. Commun.* **2011**, *2*, 292.

(16) Huang, X.; Li, S.; Wu, S.; Huang, Y.; Boey, F.; Gan, C. L.; Zhang, H. *Adv. Mater.* **2012**, *24*, 979.

(17) Huang, X.; Li, H.; Li, S.; Wu, S.; Boey, F.; Ma, J.; Zhang, H. *Angew. Chem., Int. Ed.* **2011**, *50*, 12245.

(18) Guo, Q.; Zhao, Y.; Mao, W. L.; Wang, Z.; Xiong, Y.; Xia, Y. *Nano Lett.* **2008**, *8*, 972.

(19) Sun, Y.; Yang, W.; Ren, Y.; Wang, L.; Lei, C. *Small* **2011**, *7*, 606.

(20) Zheng, H.; Cao, A.; Weinberger, C. R.; Huang, J. Y.; Du, K.; Wang, J.; Ma, Y.; Xia, Y.; Mao, S. X. *Nat. Commun.* **2010**, *1*, 144.

(21) Nie, A.; Wang, H. *Mater. Lett.* **2011**, *65*, 3380.

(22) Sun, Y.; Mayers, B.; Herricks, T.; Xia, Y. *Nano Lett.* **2003**, *3*, 955.

(23) Sun, Y. *Nanoscale* **2010**, *2*, 1626.

(24) Bagley, B. G. *Nature* **1965**, *208*, 674.

(25) Yang, C. Y. *J. Cryst. Growth.* **1979**, *47*, 274.

(26) Sun, Y.; Ren, Y.; Liu, Y.; Wen, J.; Okasinski, J. S.; Miller, D. J. *Nat. Commun.* **2012**, *3*, 971.

(27) Li, Z.; Okasinski, J. S.; Almer, J. D.; Ren, Y.; Zuo, X.; Sun, Y. *Nanoscale* **2014**, *6*, 365.

(28) Zhang, W.; Liu, Y.; Cao, R.; Li, Z.; Zhang, Y.; Tang, Y.; Fan, K. *J. Am. Chem. Soc.* **2008**, *130*, 15581.

(29) Durandurdu, M. *Phys. Rev. B* **2007**, *76*, 024102.

(30) Zhou, Y.; Fichthorn, K. A. *J. Phys. Chem. C* **2014**, *118*, 18746.

(31) Diao, J.; Gall, K.; Dunn, M. L. *Nat. Mater.* **2003**, *2*, 656.

(32) Diao, J.; Gall, K.; Dunn, M. L. *Phys. Rev. B* **2004**, *70*, 075413.

(33) Mettela, G.; Boya, R.; Singh, D.; Kumar, G. V. P.; Kulkarni, G. U. *Sci. Rep.* **2013**, *3*, 1793.

(34) Paolo, G.; Stefano, B.; Nicola, B.; Matteo, C.; Roberto, C.; Carlo, C.; Davide, C.; Guido, L. C.; Matteo, C.; Ismaila, D.; et al. *J. Phys.: Condens. Matter* **2009**, *21*, 395502.

(35) Perdew, J. P.; Zunger, A. *Phys. Rev. B* **1981**, *23*, 5048.

(36) Blochl, P. E. *Phys. Rev. B* **1994**, *50*, 17953.

(37) Baroni, S.; de Gironcoli, S.; Dal Corso, A.; Giannozzi, P. *Rev. Mod. Phys.* **2001**, *73*, 515.

(38) Our inference for the presence of non-fcc is based on powder XRD of a large number of bipyramidal crystals. Using particle counting based on SEM images and the XRD conditions employed (beam size, 1 × 10 mm; sample area, 1 × 8 mm), the total number of crystals exposed to the X-ray beam was found to be ~40,00,000 of which bipyramidal crystals were ~26,00,000.

(39) Robinson, I.; Harder, R. *Nat. Mater.* **2009**, *8*, 291.

(40) These two strained non-fcc structures are referred as bct III and bco II respectively in our theoretical study (*vide infra*).

(41) Personick, M. L.; Langille, M. R.; Wu, J.; Mirkin, C. A. *J. Am. Chem. Soc.* **2013**, *135*, 3800.

(42) Morris, J. W., Jr; Krenn, C. R. *Philos. Mag. A* **2000**, *80*, 2827.

(43) Söderlind, P.; Eriksson, O.; Wills, J. M.; Boring, A. M. *Phys. Rev. B* **1993**, *48*, 5844.

DOI: 10.1021/ja512340m
J. Am. Chem. Soc. 2015, 137, 3024−3030